

# Genesis of Hurricane Julia (2010) within an African Easterly Wave: Low-Level Vortices and Upper-Level Warming

STEFAN F. CECELSKI AND DA-LIN ZHANG

*Department of Atmospheric and Oceanic Science, University of Maryland, College Park, College Park, Maryland*

(Manuscript received 6 February 2013, in final form 28 June 2013)

## ABSTRACT

While a robust theoretical framework for tropical cyclogenesis (TCG) within African easterly waves (AEWs) has recently been developed, little work explores the development of low-level meso- $\beta$ -scale vortices (LLVs) and a meso- $\alpha$ -scale surface low in relation to deep convection and upper-tropospheric warming. In this study, the development of an LLV into Hurricane Julia (2010) is shown through a high-resolution model simulation with the finest grid size of 1 km. The results presented expand upon the connections between LLVs and the AEW presented in previous studies while demonstrating the importance of upper-tropospheric warming for TCG.

It is found that the significant intensification phase of Hurricane Julia is triggered by the pronounced upper-tropospheric warming associated with organized deep convection. The warming is able to intensify and expand during TCG owing to formation of a storm-scale outflow beyond the Rossby radius of deformation. Results confirm previous ideas by demonstrating that the intersection of the AEW's trough axis and critical latitude is a preferred location for TCG, while supplementing such work by illustrating the importance of upper-tropospheric warming and meso- $\alpha$ -scale surface pressure falls during TCG. It is shown that the meso- $\beta$ -scale surface low enhances boundary layer convergence and aids in the bottom-up vorticity development of the meso- $\beta$ -scale LLV. The upper-level warming is attributed to heating within convective bursts at earlier TCG stages while compensating subsidence warming becomes more prevalent once a mesoscale convective system develops.

## 1. Introduction

Tropical cyclogenesis (TCG) continues to be one of the least understood processes in tropical meteorology today. The formation of tropical depressions (TDs), which under favorable conditions grow into tropical storms (TSs), has many different routes, ranging from large-scale attributes such as African easterly waves (AEWs) to small-scale features taking place in mesoscale convective systems (MCSs). In particular, roughly 20% of tropical waves in the North Atlantic and eastern Pacific basins become TSs (Frank 1970). Our ability to distinguish the 20% of developing disturbances from the remaining nondeveloping disturbances in terms of factors responsible for their development is limited owing partly to the lack of high-resolution observations at the birthplace and partly to the deficiencies in current numerical weather prediction

models. Numerous theories exist to describe the multi-scale interactions that take place during TCG, but, unfortunately, it has not been until recently that such theories could be validated with field campaigns and high-resolution models.

Previous studies have referred to TCG as a two-stage problem: 1) the preconditioning of a meso- $\alpha$  and synoptic environment and 2) the construction and organization of a meso- $\beta$ -scale TC vortex (Karyampudi and Pierce 2002; Wang et al. 2010a). While these two stages might seem disjointed, they actually can occur simultaneously. The first stage involves the general environmental characteristics being favorable, such as weak vertical wind shear (VWS), warm sea surface temperatures (SSTs), sufficient column moisture content, and a low-level cyclonic rotation (Gray 1968). A vast number of synoptic-scale phenomena can provide favorable conditions for the development of TDs, ranging from equatorial waves (Schreck et al. 2012) to westerly wind bursts (Hogsett and Zhang 2010), ITCZ breakdowns (Kieu and Zhang 2009), monsoon depressions (Harr et al. 1996), and AEWs (Vizy and Cook 2009; Dunkerton et al. 2009). The

---

*Corresponding author address:* Dr. Da-Lin Zhang, Department of Atmospheric and Oceanic Science, University of Maryland, College Park, 2419 CSS Bldg., College Park, MD 20742.  
E-mail: dalin@atmos.umd.edu

North Atlantic basin is dominated by storms forming from AEWs in the main development region (MDR), even though a slim number of AEWs spawn named TSs.

A growing number of previous studies have attempted to examine the second stage of TCG with higher quality observations and modeling data. Recent studies in the Atlantic and east Pacific sectors have found an intimate relationship between TCG and AEWs (Vizy and Cook 2009; Dunkerton et al. 2009; Wang et al. 2010a; Montgomery et al. 2010) and conclude that AEWs appear to be a common type of precursor disturbances for North Atlantic TCs. However, such formation is still somewhat a mystery given the lack of understanding of multiscale interactions taking place during TCG. The role of the AEW has recently been shifted to “parent,” incubating the growth of mesoscale convective vortices (MCVs) (Dunkerton et al. 2009). The concept revolves around the notion that the predepression perturbation is protected dynamically from adverse environmental conditions such as dry air or large VWS. This idea has been further advanced by the marsupial pouch paradigm (Dunkerton et al. 2009; Wang et al. 2010a; Montgomery et al. 2010), which succinctly theorizes the preferred TCG location within an AEW. For this location to be identified using the paradigm, the AEW must be put into a comoving reference frame in which the intersection of its trough axis with its critical latitude, defined as the latitude where the zonal wind equals the phase speed of the AEW, marks the AEW’s approximate pouch center and the preferred location for development. Mesoscale perturbations that can enter this area defined by the pouch can undergo favorable development, thus providing a link between the AEW and the mesoscale perturbations. The depth and vertical alignment of the pouch is also important for development, as shown by Wang et al. (2012). Since the horizontal structure and center of the pouch depend on the phase speed of the AEW, the variance of this phase speed with height has significant implications on the growth of disturbance. While the role of the AEW in TCG has been well described via the marsupial pouch paradigm, the links between the AEW and mesoscale perturbations have been less described in the literature. It has been hypothesized that the low-level critical latitude of an AEW is a preferred location for mesoscale development (Dunkerton et al. 2009). This postulation has been investigated in limited fashion, but recent work has shown promising results on the multiscale interactions taking place during TCG (e.g., Wang et al. 2010a,b; Montgomery et al. 2012; Braun et al. 2013).

Other studies have focused on AEWs and their complex structures in relation to TCG. They include dynamical instabilities (Burpee 1972; Berry and

Thorncroft 2005), wave structures (Burpee 1972; Thorncroft and Hodges 2001; Hopsch et al. 2010), and convective development within AEWs—for example, convectively generated potential vorticity (PV) anomalies (Berry and Thorncroft 2005). It has been found that distinct differences between developing and nondeveloping AEWs include tropospheric moisture content, low-level vorticity growth, and the strength (and persistence) of deep convection within the AEW (Hopsch et al. 2010). Additionally, Wang et al. (2012) have shown that a coherent vertical structure is an important discriminating factor between developing and nondeveloping AEWs. The characteristics of developing versus nondeveloping waves lend insight into whether or not the waves are able to protect and sustain developing low-level vortices (LLVs) into TDs. The LLV is defined herein, following Zhang and Fritsch (1987), as a significant concentration of cyclonic vorticity of at least the order of magnitude of the local Coriolis parameter.

The meso- $\beta$ -scale low-level cyclonic vorticity development during TCG has been described by both the top-down (Bister and Emanuel 1997; Ritchie and Holland 1997) and bottom-up paradigms (Zhang and Bao 1996; Hendricks et al. 2004; Montgomery et al. 2006), contrasting each other in how low-level cyclonic vorticity arises. Within the top-down theory, the low-level cyclonic circulation is an extension of a preexisting midtropospheric cyclonic vortex, which may be reconstituted downward to create the surface circulation. The bottom-up theory suggests that the low-level vorticity is spun up via deep convection, which, through up-scale aggregation, becomes an LLV. The bottom-up theory has been invigorated with the concept of vortical hot towers (VHTs), which were first identified by Riehl and Malkus (1958) as “hot towers” and further conceptualized by Simpson et al. (1998) as nonrotating protected deep convective cores. Hendricks et al. (2004) and Montgomery et al. (2006) revived VHTs with the addition of vortex-tube stretching in a rotating environment. This augmentation to the bottom-up theory allows for VHTs to be the “building blocks for TCG” in which individual VHTs can conglomerate to create or enhance the LLV. Recently, both modeling and observational studies alike have been able to elaborate on VHTs and their role in TCG (Hendricks et al. 2004; Montgomery et al. 2006; Sippel et al. 2006; Houze et al. 2009).

The objectives of the present study are to (i) document the environmental conditions for the genesis of Hurricane Julia (2010) and (ii) examine the development of meso- $\alpha$ -scale surface pressure falls and a low-level vortex leading to Julia within an AEW. In this study, we examine further the hypothesis of Zhang and Zhu (2012) that upper-tropospheric processes play

an important role during TCG while demonstrating the interconnectedness of the AEW, deep convection, upper troposphere, surface pressure falls, and the LLV. The objectives are achieved through a 66-h cloud-resolving simulation of Hurricane Julia (2010) during its pregenesis stage using the Weather Research and Forecasting model (WRF) with the finest 1-km horizontal resolution. The next section provides an overview of the storm and its development within the AEW. Section 3 describes the WRF configuration and its validation while section 4 documents the formation of the LLV in relation with the AEW, upper troposphere, and persistent deep convection.

## 2. Overview

The National Hurricane Center (NHC) declared Julia a tropical depression at 0600 UTC 12 September 2010. Six hours after gaining TD status, Julia quickly became a TS. The genesis came as a surprise to NHC forecasters even with long-range guidance depicting Julia's formation several days prior (Beven and Landsea 2010). Hurricane Julia was the strongest North Atlantic hurricane east of 40°W when it reached a minimum mean sea level pressure (MSLP) ( $P_{\text{MIN}}$ ) of 948 hPa at 1200 UTC 15 September 2010. Even with this remarkable statistic, Hurricane Julia was a small, compact storm that was dwarfed by the much larger Hurricane Igor, which formed just days prior. Both storms took place during the Genesis and Rapid Intensification Processes (GRIP) (Braun et al. 2013) and the Pre-Depression Investigation of Cloud-Systems in the Tropics (PREDICT) (Montgomery et al. 2012) projects—two of the most recent observational campaigns conducted to investigate TCG. Both of these projects provided initial analysis data for the investigation of Hurricane Julia from its predepression stage even though the storm was never flown into by either project. The AEW that Julia formed within could be traced back to 0000 UTC 8 September (96 h prior to genesis) as a well-defined circulation using 600-hPa relative vorticity (Fig. 1). The westward progression of the wave is estimated to have an average phase speed ( $C_p$ ) of  $8.0 \text{ m s}^{-1}$ , which is used for the comoving frame of reference for the rest of this paper. The selection of this phase speed is calculated using the 600-hPa cyclonic vorticity Hovmöller analysis (Fig. 1) in conjunction with similar analyses from the WRF data (not shown). The most persistent closed circulation in the comoving frame was found at 600 hPa. Thus, this level was used for the phase speed calculation of the AEW. We define tropical cyclogenesis as the time when the NHC declares Julia a TD in conjunction with satisfying the condition of a closed MSLP isobar on a standard 4-hPa contouring interval of

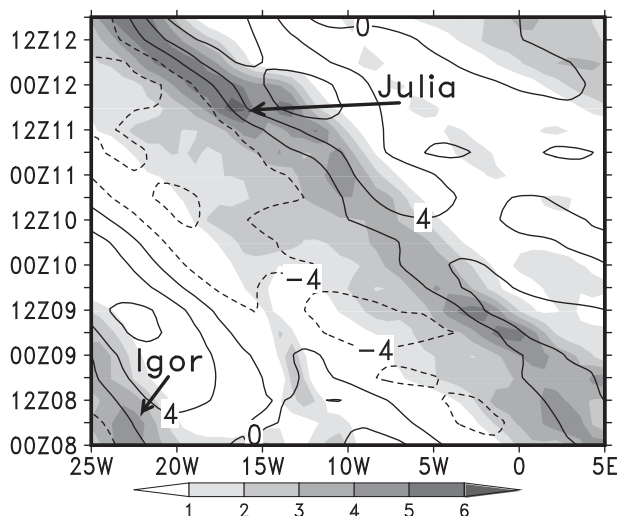


FIG. 1. Hovmöller diagram of ERA-Interim 600-hPa relative vorticity (shaded,  $10^{-5} \text{ s}^{-1}$ ) and meridional wind (contoured at interval of  $4 \text{ m s}^{-1}$ ) averaged between 8° and 13°N during the period 0000 UTC 8 Sep–1800 UTC 12 Sep 2010. The phase speed of the AEW is estimated as  $C_p = -8.0 \text{ m s}^{-1}$ . “Julia” and “Igor” mark the cyclonic vorticity associated with Hurricanes Julia and Igor, respectively.

sufficient size. The “sufficient size” constraint reassures that we do not declare TCG prematurely as a transient mesoscale feature with a closed isobar.

Hurricane Igor developed in close proximity to Julia, becoming a TD at 0600 UTC 8 September (Fig. 1). An examination of Rossby wave energy dispersion using methods similar to Li and Fu (2006) and Li et al. (2006) indicates little impact of Igor on the genesis of Julia (not shown). Given the strength of the AEW, it is not surprising that Hurricane Igor did not produce significant impact on the genesis of Julia. Perhaps its only possible impact on the TCG of Julia involved oceanic upwelling causing cooler waters to the south-southeast of the Cape Verde Islands.

At 0000 UTC 10 September, the AEW exhibited a vertically tilted closed circulation in the comoving frame as demonstrated by the circulation centers in Fig. 2a. Namely, the circulation center at 600 hPa (“X”) is seen being displaced well eastward from the upper-tropospheric circulation center (“ $X_{400}$ ”) where the cyclonic relative vorticity is maximized (Fig. 2b). Its closed circulation is identifiable down to 825 hPa (“ $X_{825}$ ”) with an open circulation below. The horizontal distance between the upper-tropospheric circulation ( $X_{400}$ ) and the lower-tropospheric disturbance ( $X_{825}$ ) is over 400 km, a testament to the complexity of the wave. The maximum cyclonic vorticity near 400 hPa is substantially higher than what has been previously observed for AEWs, which usually display a maximum between 600 and

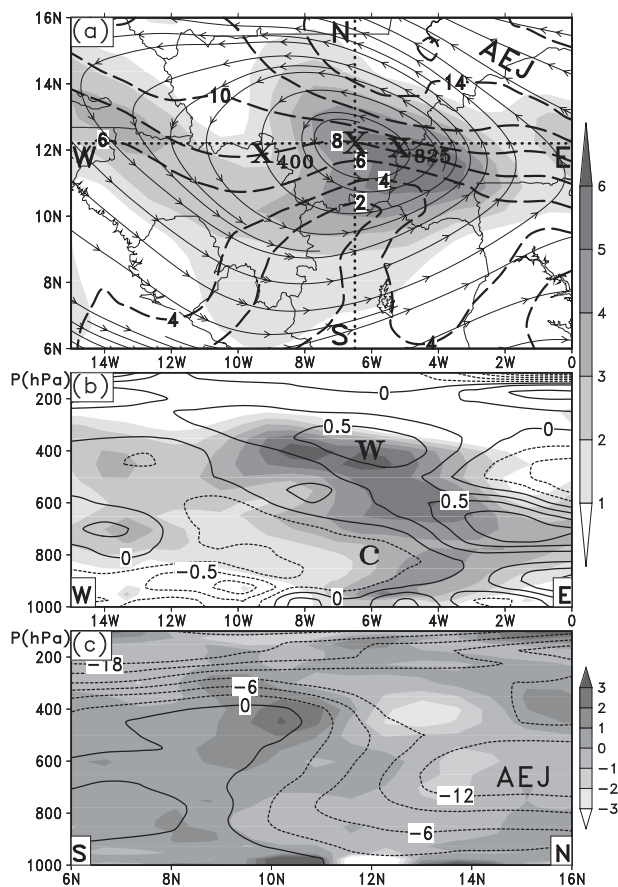


FIG. 2. (a) ERA-Interim 600-hPa relative vorticity (shaded,  $10^{-5} s^{-1}$ ), zonal wind (contoured at interval of  $2 m s^{-1}$ ), and comoving streamlines valid at 0000 UTC 10 Sep 2010. The “X” represents the intersection point of the 600-hPa trough axis and critical latitude; “X<sub>400</sub>” and “X<sub>825</sub>” represent the locations of the AEW circulation centers at 400 and 825 hPa. The dotted lines marked by W–E and S–N represent vertical cross sections shown in (b) and (c). The approximate location of the African easterly jet is marked by “AEJ.” (b) Vertical cross section of cyclonic relative vorticity (shaded,  $10^{-5} s^{-1}$ ) and temperature deviation (contoured at interval of  $0.25^{\circ}C$ ). The temperature deviation is calculated as the difference from the mean temperature at each respective level. The peak warmth and coldness associated with the AEW are marked with “W” and “C,” respectively. (c) Vertical cross section of meridional potential vorticity gradient (shaded,  $10^{-12} m s^{-1} K kg^{-1}$ ) and zonal wind (contoured at interval of  $4 m s^{-1}$ ). AEJ represents the location of the African easterly jet.

700 hPa for AEWs equatorward of  $15^{\circ}N$  (Thorncroft and Hodges 2001). The westward tilt with height of the vorticity structure is accompanied by a similar thermodynamic profile, as marked the “W” (“C”) representing the warming (cooling) above (beneath) the tilted cyclonic vorticity maximum (Fig. 2b). The 600-hPa cyclonic vorticity is mainly due to horizontal shear on the southern side of an African easterly jet (“AEJ”) (Figs. 2a,c). Baroclinic and barotropic instability can be inferred from

the reversal in the meridional PV gradient maximized near 400 hPa and to a lesser extent in the lower troposphere (Charney and Stern 1962; Burpee 1972). The combined baroclinic–barotropic instability on the synoptic scale appears to be favorable for the amplification of any mesoscale disturbance within the AEW.

The AEW under study moved due west over the 54-h period prior to TCG, traversing over the Guinea Highlands before heading over the eastern North Atlantic ocean (Fig. 3). Before its coastal passage, the AEW was dominated by sporadic weak convection (Fig. 4a), which quickly aggregated to become a large MCS as it completely moved over water at 1200 UTC 11 September (Fig. 4b). Concurrently, the Dakar rawinsonde station showed strong easterly winds in excess of  $25 m s^{-1}$  from 925 to 700 hPa (not shown) as the wave and related convection strengthened during passage. Julia quickly formed within the AEW, becoming a TD only 18 h after the wave traversed the West African coastline. By the TCG time the MCS evolved further, exhibiting a cyclonic cloud pattern (Fig. 4c) and a much more TS-like storm by 1800 UTC 12 September (Fig. 4d).

Such a short period from wave to TD has also been noted by Hopsch et al. (2010), who found that fast tropical cyclogenesis from easterly waves has higher tropospheric moisture content and larger low-level cyclonic vorticity than those of nondeveloping waves during coastal passage. A  $500 km \times 500 km$  area-averaged time series surrounding the storm center, given in Fig. 5, shows that Julia’s formation is consistent with the characteristics of fast TCG from an AEW. The simulated pre-Julia disturbance is initially tracked using the 600- and 700-hPa circulation in the comoving framework with large absolute vorticity and later using the  $P_{MIN}$  center when a mesolow becomes traceable. Specifically, precipitable waters (PW, Fig. 5a) steadily increased as the wave progressed off shore, with the strongest rises occurring when the storm was completely over water after 1200 UTC 11 September. Deep-layer vertical wind shear (850–200-hPa layer) weakened during the period and remained under  $6 m s^{-1}$  for the 36 h leading up to TCG (VWS, Fig. 5a). Post-genesis, VWS increased again to above  $8 m s^{-1}$ , possibly limiting the intensification of Julia somewhat. Cyclonic vorticity growth was predominately located at 600 hPa for the majority of the period prior to TCG, which is consistent with vorticity development in a baroclinically and barotropically unstable AEW (Hopsch et al. 2010). After 0000 UTC 12 September, the vorticity difference between 925 and 600 hPa changes sign, signifying the initiation of low-level cyclonic vorticity growth associated with the onset of genesis (Fig. 5b). Meanwhile, the AEW under study encountered sufficiently warm SSTs for tropical development, being at or above  $27^{\circ}C$ .

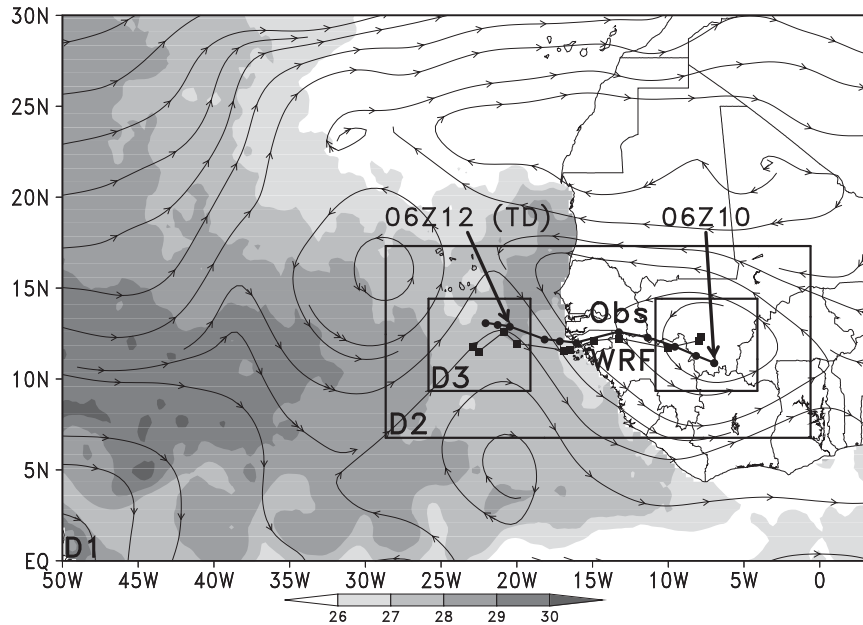


FIG. 3. WRF domain configurations: boxes D1, D2, and D3 show the domain with the horizontal resolution of 9, 3, and 1 km, respectively, with the initial and final position of the moving domain D3 also given. The WRF-simulated track (square marks) vs the best fixes track (circle marks) from 0600 UTC 10 Sep (06Z10) to 1800 UTC 12 Sep 2010 are overlaid. The NOAA OI SSTs ( $^{\circ}\text{C}$ , shaded) and ERA-Interim 600-hPa comoving streamlines at 0000 UTC 10 Sep are also overlaid.

### 3. Model description and validation

In this study, version 3.2.1 of the fully compressible, nonhydrostatic mesoscale WRF with the Advanced Research Weather (ARW) core (Skamarock et al. 2005) is used with three nests (9/3/1 km) as depicted by the boxes given in Fig. 3 (D1, D2, and D3, respectively). The nests have resolutions of 36 vertical levels<sup>1</sup> with the model top set at 50 hPa. The ARW 66-h simulation is initialized at 0000 UTC 10 September, that is, 54 h prior to the named TD Julia, and ends 1800 UTC 12 September, when the storm became a TS. The lateral boundary and initial conditions are supplied by the Interim European Centre for Medium-Range Weather Forecasts Re-Analysis (ERA-Interim) except for SSTs that are initialized by the NOAA Optimal Interpolation (OI) high-resolution SST dataset (Reynolds et al. 2007).<sup>2</sup> It should be noted that the simulation includes the NOAA OI SST data so as to gain higher spatial resolution information associated with the passage of

Hurricane Igor as Julia passed over water previously traversed by Igor. Without using high-resolution SST data, the simulated Julia is too strong given the coarser-resolution SST data not being able to resolve the cooler SSTs to the south-southeast of the Cape Verde Islands associated with Igor's passage.

The 9- and 3-km-resolution domains incorporate simultaneously the Kain-Fritsch convection parameterization scheme (Kain and Fritsch 1990; Kain 2004) and a cloud microphysics scheme, while the former is bypassed in the 1-km-resolution domain. Upon initial experimentations, we came to the conclusion that there were very little differences between two simulations with the 3-km domain having respective convection parameterized and explicitly represented. The simulation utilizes the Thompson graupel two-moment microphysics scheme (Thompson et al. 2004, 2008), the Rapid Radiative Transfer Model (RRTM) longwave radiation scheme (Mlawer et al. 1997), the Dudhia (1989) shortwave radiation scheme, and the Yonsei University (YSU) planetary boundary layer (PBL) scheme (Noh et al. 2003).

The 1-km moving domain has 570 preset moves starting 9 h after the initialization time. Easterly moves are conducted every 6 min to follow the AEW and involves no movement of the domain latitudinally. Preset

<sup>1</sup>The vertical levels are clustered in the lower and upper troposphere to gain greater vertical resolution where the confluent and diffluent motions are most present during genesis.

<sup>2</sup>NOAA OI SSTs remain fixed for the integration as the SSTs remain nearly constant over the 66-h period.

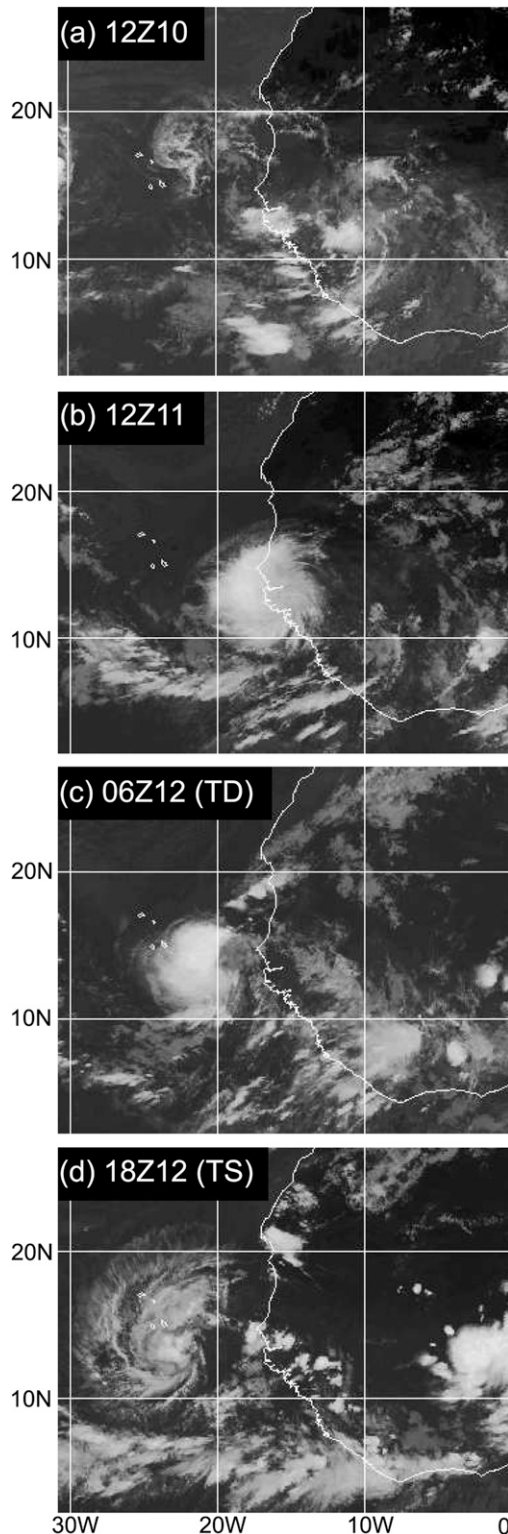


FIG. 4. *Meteosat-9* IR imagery for four stages of Hurricane Julia: (a) sporadic convection within the AEW at 1200 UTC 10 Sep, (b) well-defined MCS within the AEW at 1200 UTC 11 Sep, (c) TD at 0600 UTC 12 Sep, and (d) TS at 1800 UTC 12 Sep 2010.

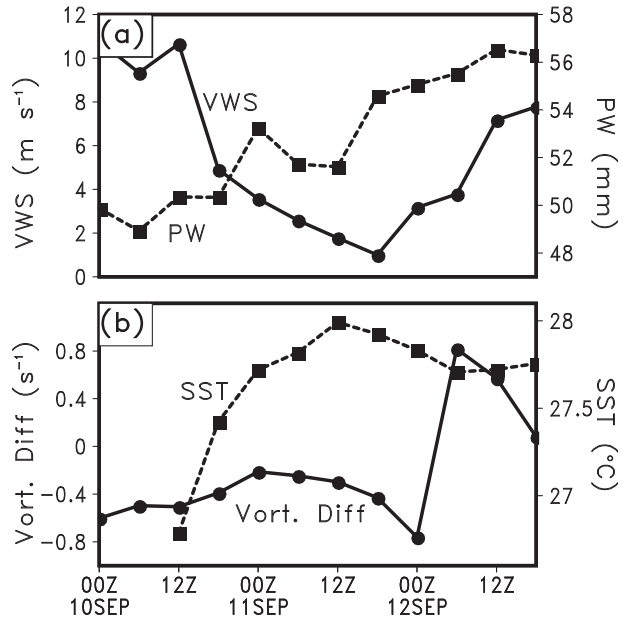


FIG. 5. Time series of (a) deep-layer vertical wind shear (VWS) between 200 and 850 hPa and precipitable water (PW) and (b) 925–600-hPa relative vorticity difference ( $\zeta_{925} - \zeta_{600}$ ) and SST during the 66-h period from 0000 UTC 10 Sep to 1800 UTC 12 Sep 2010. Each variable is calculated by averaging its field within a 500 km  $\times$  500 km area from the storm center using ERA-Interim data.

moves are used since the vortex-following tool associated with the ARW has trouble following the AEW with tracking levels at 600 hPa, even given the relatively strong AEW.

Overall, the WRF simulation reproduces reasonably well the observed track over the 66-h integration (Fig. 3). On average, the simulated track error is 173 km, but its operational 36-h forecast did significantly better than the NHC official (OFCL) forecast track error for the same time (Beven and Landsea 2010), with a track error of 94 km compared to the OFCL forecast error of 133 km. The intensification of predepression Julia was unremarkable, reaching a  $P_{\text{MIN}}$  of 1007 hPa at the TCG time as seen in observed  $P_{\text{MIN}}$  estimates (Fig. 6). The simulated  $P_{\text{MIN}}$  and maximum wind speed at  $z = 10$  m ( $V_{\text{MAX}}$ ) both agree well with the observed, although they are not without discrepancies. One difference is that the simulated surface vortex is 2 hPa weaker than the observed during the first 12 hours of integration and is 2 hPa stronger at TCG.

Two development stages can be identified from the  $P_{\text{MIN}}$  changes: (i) TCG and (ii) significant intensification (SI) prior to and after 0600 UTC 12 September, respectively. Specifically, the  $P_{\text{MIN}}$  of the disturbance during TCG barely changes, with an average deepening rate of  $1 \text{ hPa day}^{-1}$ . In contrast, the SI phase begins with

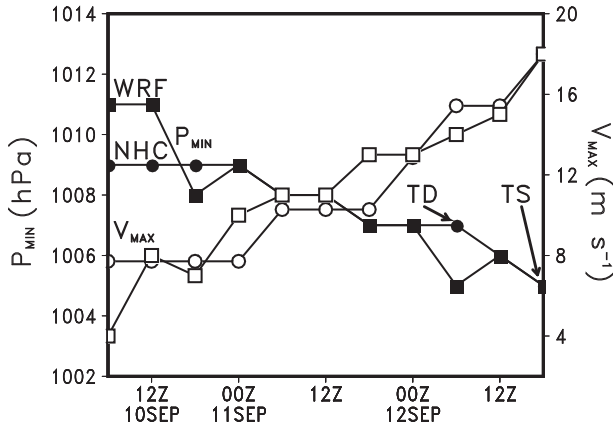


FIG. 6. Time series of the WRF-simulated storm intensity (square marks) and the NHC best estimates (circle marks) for the minimum MSLP ( $P_{MIN}$ , closed marks) and  $z = 10$ -m maximum wind speed ( $V_{MAX}$ , open marks) from 0600 UTC 10 Sep to 1800 UTC 12 Sep 2010.

the deepening rate increasing to  $4 \text{ hPa day}^{-1}$  until the storm becomes a TS, similar to the results of Nolan (2007). The simulated MSLP prematurely enters SI at 0000 UTC 12 September, with a deepening of 2 hPa for the 6 h prior to the storm becoming a named TD. Later in the SI stage, the simulated  $P_{MIN}$  shows brief weakening before restrengthening at 1800 UTC 12 September. This reprieve is supported by the decrease in SSTs and increase in VWS shown in Fig. 5, which can inhibit intensification. While these developmental stages are evident in  $P_{MIN}$ , they cannot be seen from the 10-m maximum wind speed as both observations and simulation show a nearly consistent increase during the 66-h integration.

Figure 7 shows the simulated cloud patterns of the AEW (and Julia) that should be compared to the observed *Meteosat-9* IR imagery given in Fig. 4. The simulated brightness temperatures are calculated using the Unified Post Processor (UPP), which invokes the Community Radiative Transfer Model (CRTM) to produce brightness temperatures at the top of the atmosphere. After 12 h into the integration, the model reproduces the locations of deep convection along the coastline, indicating reasonable forcing within the AEW. However, the simulated cloud field associated with the AEW appears to be weaker and more fragmented than the observed (cf. Figs. 4a and 7a), owing partly to the lack of precipitation spinup and partly to the simulated upper-level cloud ice content that may be much less than that in nature. The differences between the simulated and observed cloud patterns decrease afterward. By 1200 UTC 11 September (cf. Figs. 4b and 7b), the simulated brightness temperatures show well

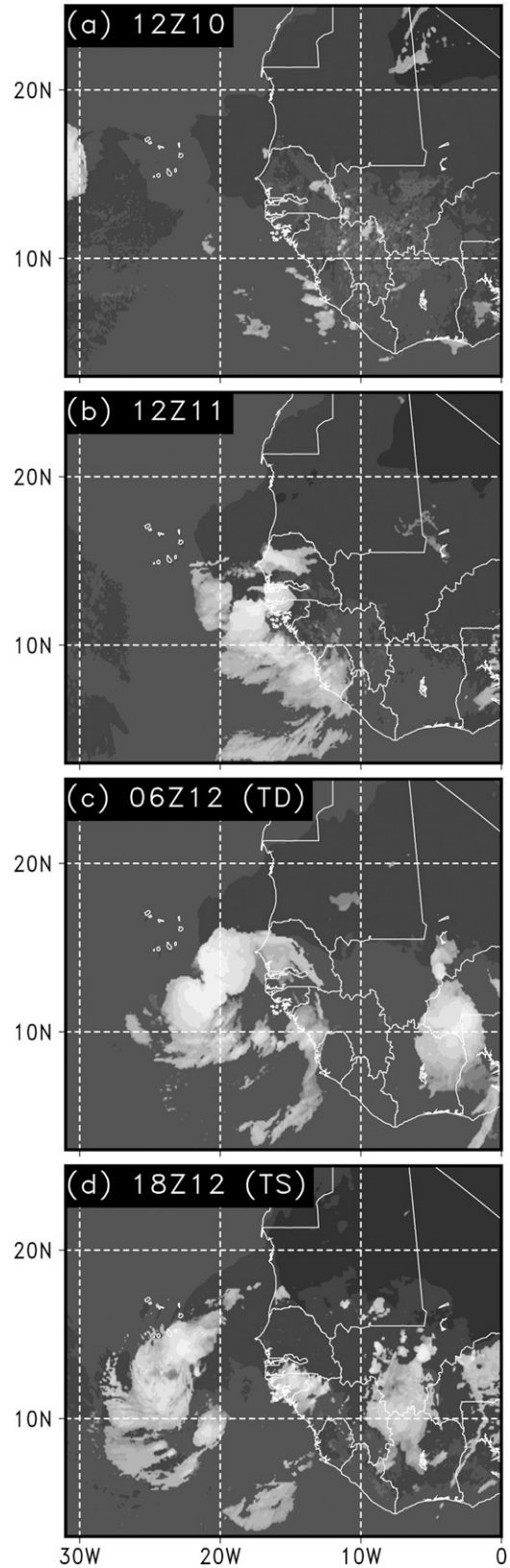


FIG. 7. As in Fig. 4, but for the WRF-simulated brightness temperature (K).

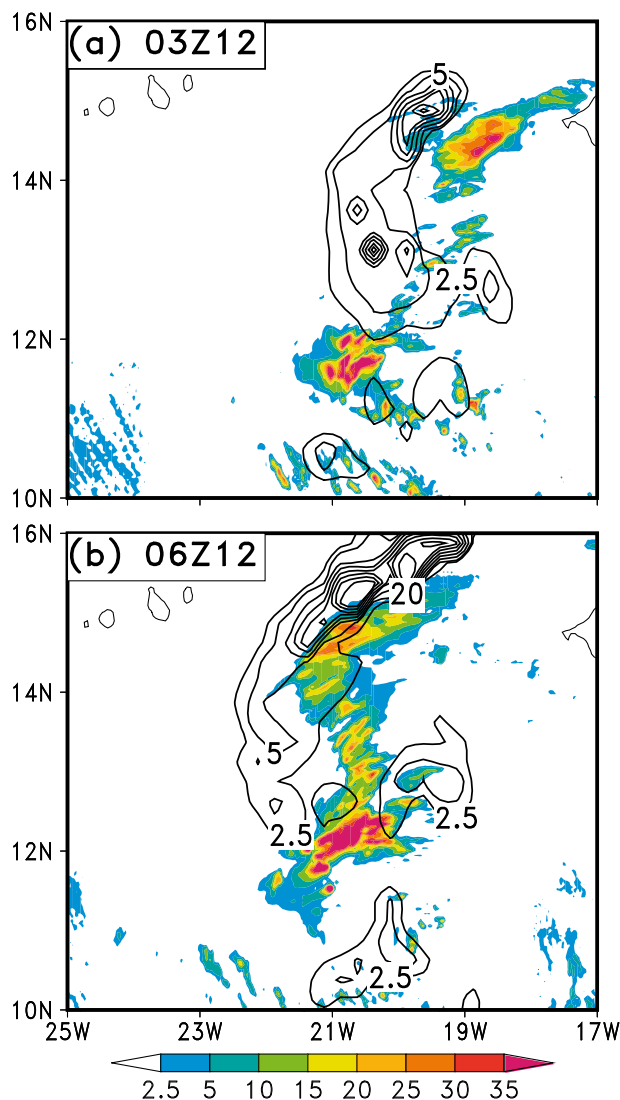


FIG. 8. Comparison of the WRF-simulated hourly precipitation rate (shaded,  $\text{mm h}^{-1}$ ) and TRMM-adjusted merged-infrared precipitation rate (contoured at 2.5, 5, 10, 15, 20, 25, 30, and  $35 \text{ mm h}^{-1}$ ) for (a) 0300 and (b) 0600 UTC 12 Sep 2010. The 3-km horizontal-resolution WRF data is used while the TRMM data has a horizontal resolution of  $0.25^\circ \times 0.25^\circ$ .

the convective development along the coastline, although it does not look like the round-shaped MCS as seen in *Meteosat-9* IR imagery. The WRF nearly reproduces the observed brightness temperatures of TD Julia at 0600 UTC 12 September. Even with the slow convective development during the early stages, the WRF simulates a TS-like cloud pattern at 1800 UTC 12 September that compares favorably with the observed (Fig. 7d).

Since we are concerned with mesoscale development in addition to the AEW, Fig. 8 compares the simulated hourly precipitation rates ( $\text{mm h}^{-1}$ ) to the Tropical

Rainfall Measuring Mission (TRMM) data at 0300 and 0600 UTC 12 September. The TRMM data consists of precipitation rate estimates generated every 3 h on a  $0.25^\circ \times 0.25^\circ$  grid between  $50^\circ\text{S}$  and  $50^\circ\text{N}$ . We show comparisons at the two aforementioned times to validate that the convective coverage is reasonable during the early stages of simulated SI, our period of focus in the following sections. The overall spatial characteristics of the TRMM-estimated precipitation rates compare favorably with the simulated, although some minor discrepancies on the location of heavy precipitation rates are evident. At 0300 UTC 12 September, the TRMM estimate depicts a more coherent, MCS-like structure while the simulated shows two distinct precipitation areas with little convective development in between (Fig. 8a). Even with this disagreement, the intensity of the simulated rates fares well with the TRMM, highlighting small regions of intense precipitation in excess of  $30 \text{ mm h}^{-1}$ . By 0600 UTC 12 September, the simulated rates pick up on the MCS-like structure shown in TRMM estimates with little spatial disagreement. However, the simulation seems to be overestimating the precipitation rates on the southern end of the feature with a broad swath of  $30 \text{ mm h}^{-1}$  or greater rates (Fig. 8b). This is contrasted by a reasonable estimate of the heavy precipitation rates on the northern portion of the feature shown in TRMM estimates. In general, the characteristics of the TRMM precipitation rates are reasonably reproduced by the simulation for the 3-h period between 0300 and 0600 UTC 12 September when discounting minor spatial displacements and the differences in resolution between the two datasets.

#### 4. Low-level development and upper-level processes

After verifying the simulated storm against the observed, we can use the high-resolution simulation data to examine the development of some nonobservable features, especially the meso $\beta$ -scale LLV that becomes TD Julia. In this section, we show that the LLV develops within the parent AEW, but they are not directly collocated until into the simulated storm's SI stage. In particular, we show that the LLV formation results from persistent deep convection and its generated vortices, upper-tropospheric warming, and vorticity growth in the lower troposphere. The AEW serves as the parent in a deep layer, similar to that described by the marsupial pouch paradigm (Dunkerton et al. 2009; Wang et al. 2010a; Montgomery et al. 2010), protecting the upper-level warming and the LLV from adverse environmental conditions while providing a preferred location for mesoscale development.

*a. Connecting the AEW to MSLP falls, upper-level warming, and the LLV*

Figure 9 presents the evolution of meso- $\alpha$ -scale MSLP falls, a meso- $\beta$  surface low (marked by “L”), the LLV, and AEW. A closed MSLP isobar (“L”) first appears within the AEW at 0000 UTC 12 September (Fig. 9a). This closed isobar, however, is considered to be a meso- $\beta$  low rather than TD Julia since its size is comparable to other meso- $\beta$  features. Even though the simulated storm is not a TD-scale disturbance until 0600 UTC 12 September (Fig. 9c), the remainder of the paper will refer to the simulated SI starting at 0000 UTC 12 September since an intensifying surface low is identifiable. Initially, the mesolow and the AEW center (marked by “X”) are separated by a distance of approximately 150 km (Fig. 9a). This distance remains nearly constant until 0600 UTC 12 September as the surface low deepens. After this time during SI, the distance between the two centers shrinks to about 100 km (Fig. 9c), and the centers become nearly collocated at 0900 UTC 12 September (Fig. 9d).

This change in distance over the 9-h period can be more clearly seen from the vertical vorticity structures of the two disturbances in Figs. 9e–h. Initially, the dominant vorticity feature is that of the AEW (its peak denoted by “A”) and is maximized between 700 and 400 hPa at 0000 UTC 12 September (Fig. 9e). A deep upright column of cyclonic vorticity associated with the meso- $\beta$  surface low emerges at the edge of the tilted vorticity column associated with the AEW by 0300 UTC 12 September, with its peak magnitude exceeding that of the AEW (Fig. 9f). At this time, the mesolow has cyclonic relative vorticity well in excess of  $3 \times 10^{-5} \text{ s}^{-1}$  and, as such, can be considered a low-level vortex by definition. By comparison, the AEW vorticity exhibits little change during the past 54 h (cf. Figs. 2b and 9e–h). While the LLV is intensifying with time, it begins to merge with the vertically tilted AEW vortex from the top. Although the mesolow signifies the beginning of the SI stage at 0000 UTC 12 September (Fig. 6), the LLV merges into the AEW vortex center near 0900 UTC 12 September (Figs. 9d and 9h).

Even with the near constant intensity of the AEW over the 54-h period, its MSLP field and intensity show significant changes due to the development of deep convection (to be shown later), with the majority of changes taking place between 0000 and 0900 UTC 12 September. In addition to the local MSLP falls associated with the meso- $\beta$  surface low (“L”), one can see spatial expansion of the MSLP falls with time from the meso- $\beta$  to meso- $\alpha$  scale. This is easily exemplified by the 1008-hPa isobar in Figs. 9a–d, which continually expands until 0600 UTC 12 September before contracting slightly

at 0900 UTC 12 September. The evolution of the meso- $\alpha$ -scale MSLP falls during the simulated SI is of interest to this study.

Figures 9e–h show that the intensification of the meso- $\beta$  surface low and meso- $\alpha$  MSLP falls are accompanied by thermodynamic changes in the upper troposphere. Initially, the only evident thermodynamic profile is that of the AEW, with a tilted warm layer above the midlevel vortex marked by “W” in Fig. 9e. This tilted profile quickly diminishes as warmth in excess of  $2^\circ\text{C}$  takes place directly above the developing LLV (“W”, Fig. 9f). The warming above the LLV extends back over the top the AEW’s cyclonic vorticity, merging with the warm layer above the midlevel vortex. The warmth above the LLV continues to intensify until 0900 UTC 12 September when the thermodynamic profile associated with the AEW is no longer identifiable and upper-tropospheric warmth exceeds  $2.5^\circ\text{C}$  (Fig. 9h).

While the AEW pouch center has been shown to be the sweet spot for the growth of mesovortices according to Dunkerton et al. (2009), our results show that the intensification of the meso- $\beta$ -scale surface low and LLV initially occurs 100–150 km away from the pouch center. The collocation of the two does not occur until well into significant intensification, though the amplification of the mesoscale features does occur in close proximity to the pouch center. This suggests that unlike the vortex merging of Kieu and Zhang (2009), the SI of TCs within AEWs may occur before a vertically coherent vortex forms. It is worth mentioning that the pouch center can also include some arbitrary area surrounding the intersection point of the AEW trough axis and critical latitude. Thus, the point location of the intersection is not the only favorable location for TCG. Even so, the merging of the LLV and AEW is realized by the bottom-up growth of cyclonic vorticity associated with the LLV (Zhang and Bao 1996; Hendricks et al. 2004; Montgomery et al. 2006) and the midlevel cyclonic vorticity of the AEW.

*b. Meso- $\alpha$  and meso- $\beta$  MSLP falls and their relationship to upper-level warming and deep convection*

While the preceding subsection demonstrates some relationship between the AEW, the meso- $\beta$  surface low, LLV, and upper-tropospheric warming, an obvious question to ask is how do these features interact? The following will answer this question in addition to determining what role, if any, the warming seen in Figs. 9e–h has on MSLP falls at both meso- $\alpha$  and meso- $\beta$  scales. In this regard, we note the observational study of Hoxit et al. (1976) showing that upper-level warming (in the 100–500-hPa layer) associated with deep convection in midlatitude MCSs could produce surface pressure falls

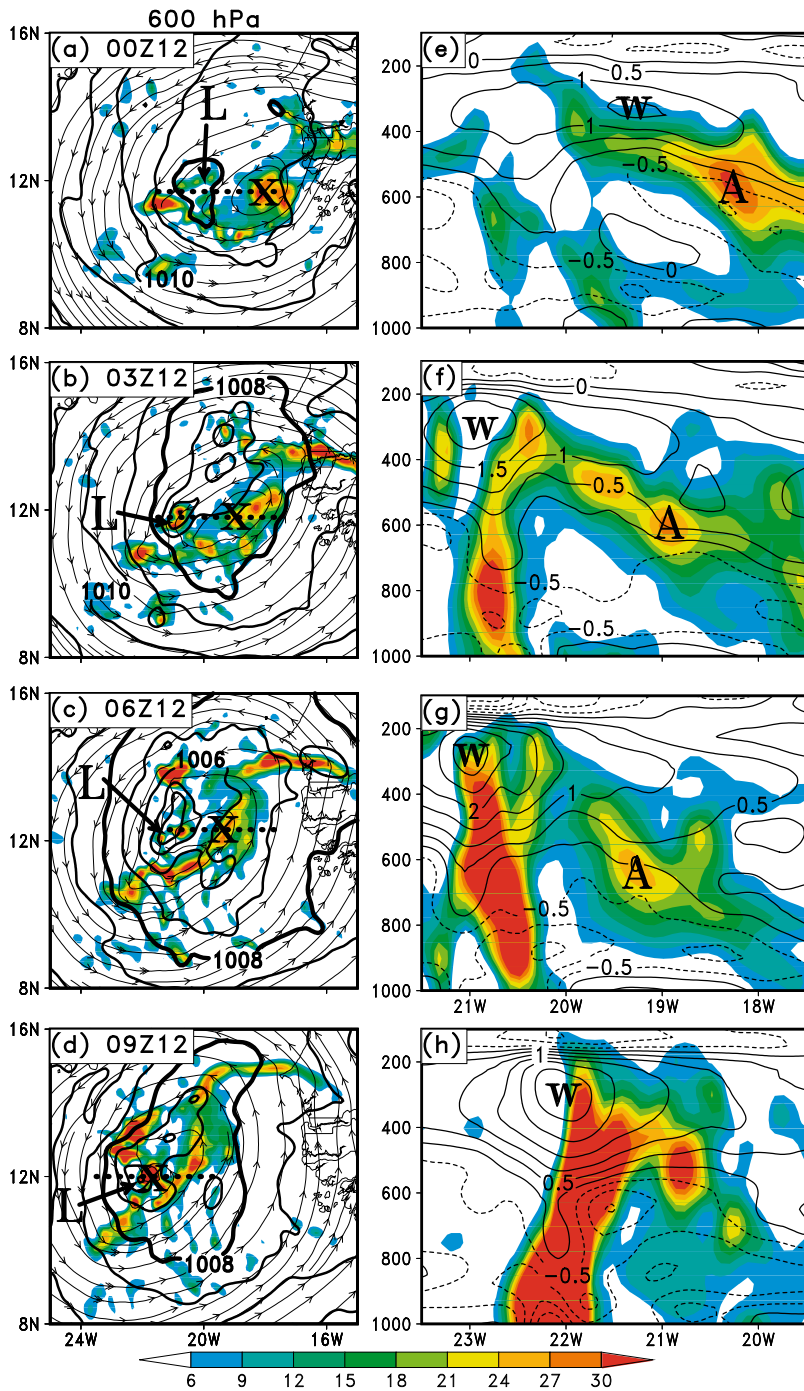


FIG. 9. (a)–(d) The simulated 600-hPa cyclonic relative vorticity (shaded,  $10^{-5} \text{ s}^{-1}$ ), comoving streamlines, and MSLP (contoured at interval of 1 hPa). The “L” represents the center of a developing mesolow while the intersection of the 600-hPa trough axis and critical latitude is marked with the “X.” The dotted line designates the west–east cross sections shown in (e)–(h). (a)–(c) span the same longitudes listed below (d). (e)–(h) Longitude–height cross sections of cyclonic relative vorticity (shaded,  $10^{-5} \text{ s}^{-1}$ ) and temperature deviations (contoured at interval of  $0.5^\circ\text{C}$ ) that are calculated by subtracting the mean temperature at each level of the cross section. “A” represents the location of the peak cyclonic vorticity associated with the AEW while “W” marks the location of the upper-level warming. The cross section length in (e)–(h) is approximately 400 km starting at  $21.5^\circ$  and ending at  $17.5^\circ\text{W}$ , with the exception of (h), which extends from  $23.5^\circ$  to  $19.5^\circ\text{W}$ . The cross sections are created using a three-slice average. Data from the WRF 9-km-resolution domain were used to create all panels.

of  $2\text{--}4\text{ hPa h}^{-1}$ . They attributed meso- $\beta$ -scale surface lows to the hydrostatic warming aloft. Similarly, Zhang and Zhu (2012) have shown the importance of the upper-tropospheric warming in TCG, demonstrating that the warming prior to TCG accounts for the majority of the MSLP falls. They hypothesize that the upper-tropospheric warming is produced by widespread deep convection that detrains just below the tropopause and then by outward advection through divergent flows. The following will only focus on the 3 h between 0300 and 0600 UTC 12 September when the MSLP falls are the greatest at approximately  $0.67\text{ hPa h}^{-1}$  (Figs. 9a–d) and the development of the LLV occurs.

Figures 10a–h show that the MSLP falls are consistently collocated with the warmer air at 200 hPa along the AEW's critical latitude at 925 hPa during the 3-h period. Additionally, these MSLP falls are associated with the region of active convection shown in Fig. 8. We use the 1006-hPa isobar and the  $-52.5^\circ\text{C}$  isotherm to help explain this relationship. As the  $-52.5^\circ\text{C}$  isotherm expands outward over the period into a meso- $\alpha$ -scale feature, so does the 1006-hPa isobar, which nearly takes the same shape and size as the warm regions at 200 hPa. Within the meso- $\alpha$ -scale MSLP falls, smaller meso- $\beta$  and meso- $\gamma$   $P_{\text{MIN}}$  centers reside beneath the warmest temperatures at 200 hPa, with examples marked by "L" in Figs. 10a–d. An exceptional occurrence of such a feature occurs at 0400 UTC 12 September when a 1004-hPa MSLP closed contour develops directly beneath 200-hPa temperatures in excess of  $-49^\circ\text{C}$  (Fig. 10b). The concurrent development of the 200-hPa warming and the meso- $\alpha$  MSLP falls supports the notion that the warming may be hydrostatically responsible for the intensity and size of the MSLP disturbance. These features can be linked to the development, intensification, and aggregation of convection along the AEW low-level critical latitude, as explained next via Figs. 10e–h.

It is seen in the composite radar reflectivity that the development of deep convection occurs in the same regions as the warming at 200 hPa as well as along the AEW's low-level critical latitude (Figs. 10e–h). Since deep convection (either as individual convective cells or a mesoscale convective vortex) tends to move with the AEW when it resides on the AEW low-level critical latitude (Dunkerton et al. 2009), it is able to persistently detrain in the upper troposphere, allowing for the warming to intensify and advect radially outward as a storm-scale outflow develops. The streamline analyses in Figs. 10a–d support the outward expansion of the warming in time, with a storm-scale outflow developing by 0600 UTC 12 September. Initially, this outflow is less coherent (e.g., 0300 UTC 12 September), resulting in similar patterns of upper-level warming and surface

pressure falls. Once deep convection becomes organized along the AEW low-level critical latitude, a storm-scale outflow develops, expanding the upper-tropospheric warming and allowing for MSLP falls on the meso- $\alpha$  scale.

Figures 10e–h show the relationship between the meso- $\beta$ -scale surface pressure falls and the development of low-level cyclonic vorticity. Initially, two noticeable mesovortices (" $V_1$ " and " $V_2$ ") reside within meso- $\beta$ -scale MSLP lows and, consequently, in regions where the PBL convergence is enhanced as evidenced by the comoving streamline analysis (Fig. 10e). The mesovortices intensify via vortex stretching, noted by the presence of convection and related upward motions (Figs. 10e–h). A notable characteristic of  $V_2$  is its radial movement along the low-level critical latitude (Figs. 10e–h). This vortex starts off nearly 200 km from the AEW center at 0300 UTC 12 September but cascades toward the AEW center along the critical latitude as it begins to merge with  $V_1$  at 0600 UTC 12 September. The interaction of the two at 0600 UTC 12 September represents the conglomeration and homogenization of the 925-hPa cyclonic vorticity field with the creation of the meso- $\beta$ -scale LLV. Additionally, the enhancement of the vortices is consistently along the critical latitude of the 925-hPa AEW circulation near the pouch center (Figs. 10e–h), validating the connection between the meso and larger-scale circulations postulated by Dunkerton et al. (2009). The LLV by 0600 UTC 12 September also starts to take the shape of the meso- $\beta$ -scale surface low encompassed by the 1006-hPa isobar (Fig. 10h), hinting that its amplification is partly explained by the surface pressure falls induced by the warming aloft.

To further analyze the evolution of the upper-tropospheric warming, Fig. 11a presents a  $100\text{ km} \times 100\text{ km}$  area-averaged time series following the storm center of cyclonic vorticity and relative warming with respect to the vertical temperature profile at 0600 UTC 11 September.<sup>3</sup> We can see two distinct warming periods from Fig. 11a: (i) a shallow intense warming event in the layer above 250 hPa during the first 18 h with a peak intensity near  $1.25^\circ\text{C}$  at 1500 UTC 11 September and (ii) a deep-layer warming event in association with the onset of SI after 0000 UTC 12 September. The first warming period is in good agreement with the early sporadic convection within the AEW when the latter moves across the coastline (Figs. 7a,b) and the system is dominated by the midlevel cyclonic vortex (AEW in Fig. 11a). The localized nature of the deep convection is

<sup>3</sup> A  $100\text{ km} \times 100\text{ km}$  average is used to accurately capture the critical information related to TCG as noted by Wang (2012).

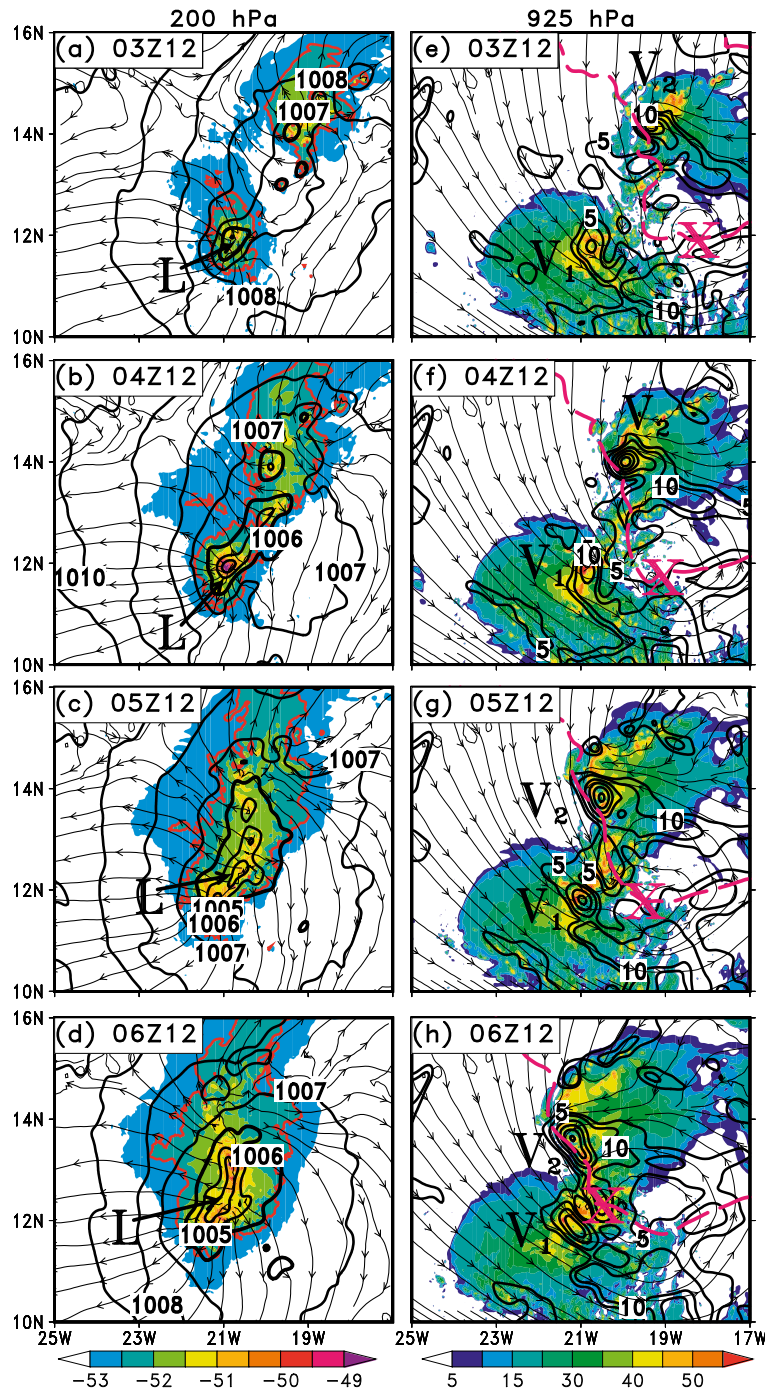


FIG. 10. (a)–(d) The simulated 200-hPa temperature (shaded, °C), comoving streamlines, and MSLP (contoured at interval of 1 hPa) from the 51–54-h integrations, valid at 0300, 0400, 0500, and 0600 UTC 12 Sep, respectively. The  $-52.5^{\circ}\text{C}$  isotherm is outlined in thick red to show the expansion of the warmth while the 1006-hPa isobar is thickened to demonstrate the expansion of the mesolow. The “L” represents the center of a developing meso- $\beta$  surface low. (e)–(h) The simulated composite radar reflectivity (shaded, dBZ), 925-hPa cyclonic relative vorticity (contoured at interval of  $5 \times 10^{-5} \text{ s}^{-1}$ ), comoving streamlines, and AEW latitude (magenta dashed line) for (a)–(d).  $V_1$  and  $V_2$  represent the two main meso- $\beta$ -scale vortices that become the LLV. The intersection of the 925-hPa AEW trough axis with its respective critical latitude is marked with the magenta “X”. Data from the WRF 3-km-resolution domain were used to create all panels.

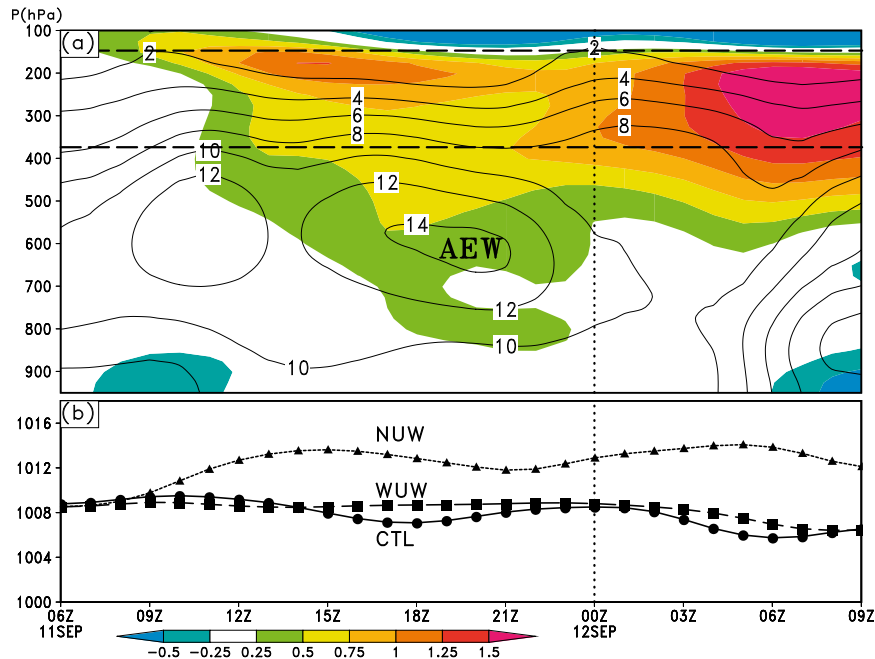


FIG. 11. (a) Time–height cross section of the simulated temperature difference from the 30-h simulated (valid at 0600 UTC 11 Sep, shaded, °C) and cyclonic relative vorticity (contoured at interval of  $2 \times 10^{-5} \text{ s}^{-1}$ ) that are obtained using a  $100 \text{ km} \times 100 \text{ km}$  average surrounding the storm center. Dashed lines represent the core of the upper-level warming and “AEW” marks the peak cyclonic vorticity associated with the AEW. (b) Time series of the  $100 \text{ km} \times 100 \text{ km}$  area-averaged MSLP (hPa) from the WRF simulation (CTL) and two hydrostatic calculations (NUW and WUW). The NUW hydrostatic calculation uses the vertical temperature profile from 0600 UTC 11 Sep between the dashed lines in (a) while WUW utilizes the 0600 UTC 11 Sep profile plus the temperature perturbations between the dashed lines seen in (a). The dotted lines in both (a) and (b) represent the time SI begins for the simulated storm: 0000 UTC 12 Sep. Data from the WRF 1-km-resolution domain were used to create both panels.

relatively less efficient at generating larger-scale warming in the upper-troposphere since a coherent storm-scale outflow is not present. The second warming period starts at 0000 UTC 12 September when the onset of SI takes place. This period is marked by steady warming in the 375–150-hPa layer (Fig. 11a), in agreement with the warming shown above the developing meso- $\beta$  surface low and LLV in Figs. 10e–h and 9a–d. This warming increases in both intensity and depth with an amplitude exceeding  $1.5^\circ\text{C}$  at and after 0600 UTC 12 September. Development of the LLV can be seen in the 950–700-hPa layer after 0300 UTC 12 September coinciding with the increased upper-level warming and MSLP falls seen in Figs. 9 and 10.

Quantifying the importance of the upper-level warming for surface pressure falls, Fig. 11b is plotted following the procedures similar to those described in Chen and Zhang (2013), in which (i) the MSLP is obtained by calculating the hydrostatic equation from the tropopause downward using the total temperature (i.e., the sum of the temperature profile at 0600 UTC

11 September and the warming, curve WUW) and (ii) repeating (i) but excluding the upper-level warming enclosed by the dashed lines, curve NUW. The control-simulated time series of MSLP (curve CTL) is also given to facilitate the comparison between the two different calculations. Obviously, the NUW time series struggles to reproduce the MSLP of the control simulation and diverges from the other solutions after 0900 UTC 11 September. The differences between NUW and CTL maximize after 0000 UTC 12 September when the convective activity becomes more coherent and the subsequent warming starts to induce more pronounced MSLP falls. The difference between the two reaches a peak of nearly 10 hPa as the NUW time series never develops a tropical depression. Contrasting its counterpart, the WUW hydrostatic calculation is nearly able to fully reproduce the CTL time series. The difference between the CTL and WUW is never greater than 2.5 hPa, demonstrating the importance of the upper-tropospheric warming for MSLP falls and the intensification of the meso- $\beta$  surface low.

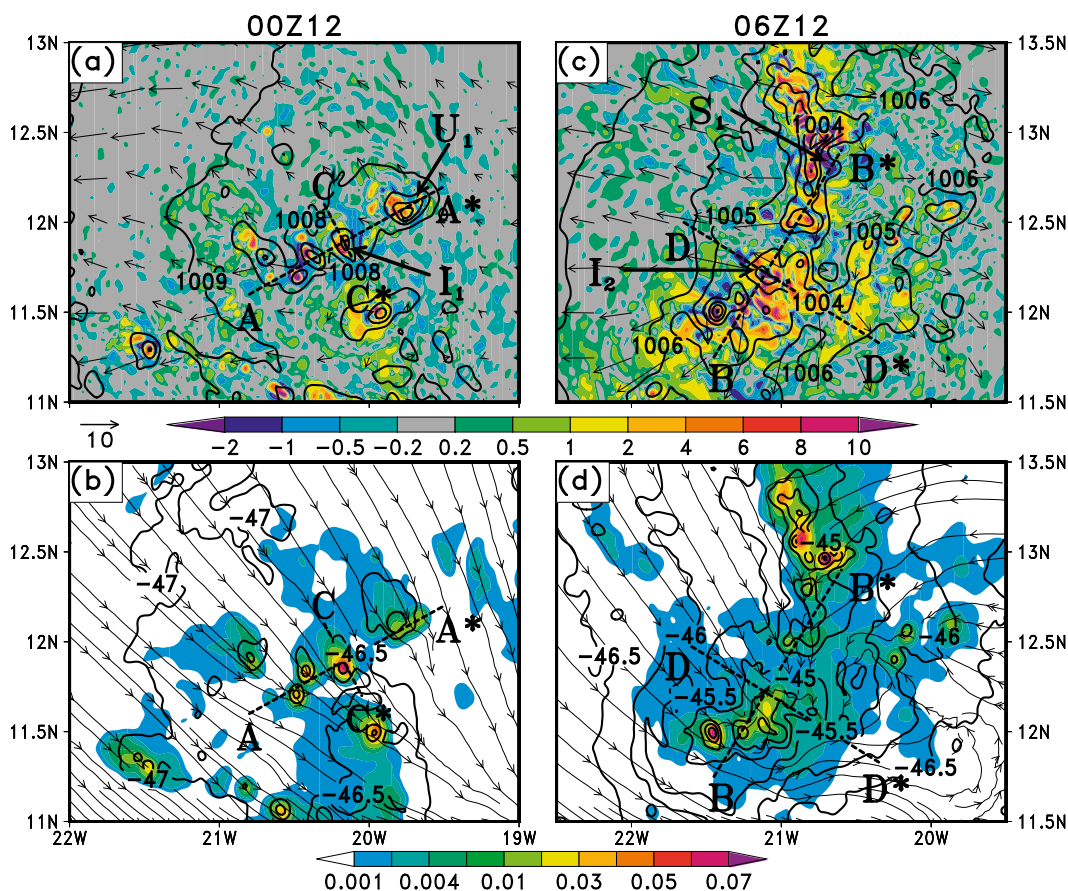


FIG. 12. (a),(c) Simulated 275–175-hPa layer-averaged vertical velocity (shaded,  $\text{m s}^{-1}$ ) and comoving wind vectors ( $\text{m s}^{-1}$ ) with MSLP (contoured at interval of 1 hPa) overlaid for 0000 and 0600 UTC 12 Sep, respectively. (b),(d) Simulated 275–175-hPa layer-averaged cloud ice mixing ratio (shaded,  $\text{g kg}^{-1}$ ) and temperature (contoured at interval of  $0.5^\circ\text{C}$ ) with 925-hPa comoving streamlines overlaid for the same times as in (a) and (c), respectively. Dashed lines labeled A–A\*, B–B\*, C–C\*, and D–D\* represent the locations of vertical cross sections shown in Fig. 13. Cross sections A–A\* and B–B\* are created along the main axis of the MSLP disturbance while C–C\* and D–D\* are created along the short axis of the MSLP disturbance. The other letters in (a) and (c) represent the intersection of the respective cross sections ( $I_1$  and  $I_2$ ), the location of a CB and related  $P_{\text{MIN}}$  ( $U_1$ ), and a location of compensating subsidence warming ( $S_1$ ).  $I_2$  also represents an area of compensating subsidence warming associated with a  $P_{\text{MIN}}$ . Data from the WRF 1-km-resolution domain were used to create (a)–(d).

### c. The development of the upper-level warming

After seeing a connection between upper-level warming, the meso- $\alpha$ -scale MSLP falls, the meso- $\beta$ -scale surface low, and the LLV in the preceding subsections, we show below how the upper-level warming forms. Chen and Zhang (2013) showed that adiabatic subsidence resulted in the development of an upper-level warm core during the rapid intensification stage of Hurricane Wilma. While large-scale adiabatic subsidence warming might be true for a mature TC, how the upper-tropospheric warming during TCG forms remains unanswered. Of particular interest herein are the meso- $\gamma$ -scale features—namely, convective bursts (CBs) and their influence on the upper-level warming. Traditionally,

CBs are defined as intense meso- $\gamma$  convective cells with updrafts maximized in the upper troposphere. The method by which a CB is defined is rather arbitrary, with the updraft velocity threshold being anywhere from 8 to  $15 \text{ m s}^{-1}$ , as used in Chen and Zhang (2013). For our investigation, we will designate a convective cell as a CB when it is characterized by an updraft in excess of  $8 \text{ m s}^{-1}$  at or above the freezing level ( $\sim 600 \text{ hPa}$ ).

Focusing on 0000 UTC 12 September (onset of SI, Figs. 12a,b), the meso- $\beta$ -scale surface low is characterized by embedded meso- $\gamma$ -scale structures beneath upward motions aloft (red shadings). An example of such a meso- $\gamma$  low and its associated upward vertical motion is marked by “ $U_1$ .” Applying our definition of CBs, it is clear that many of the meso- $\gamma$  structures are CBs, with

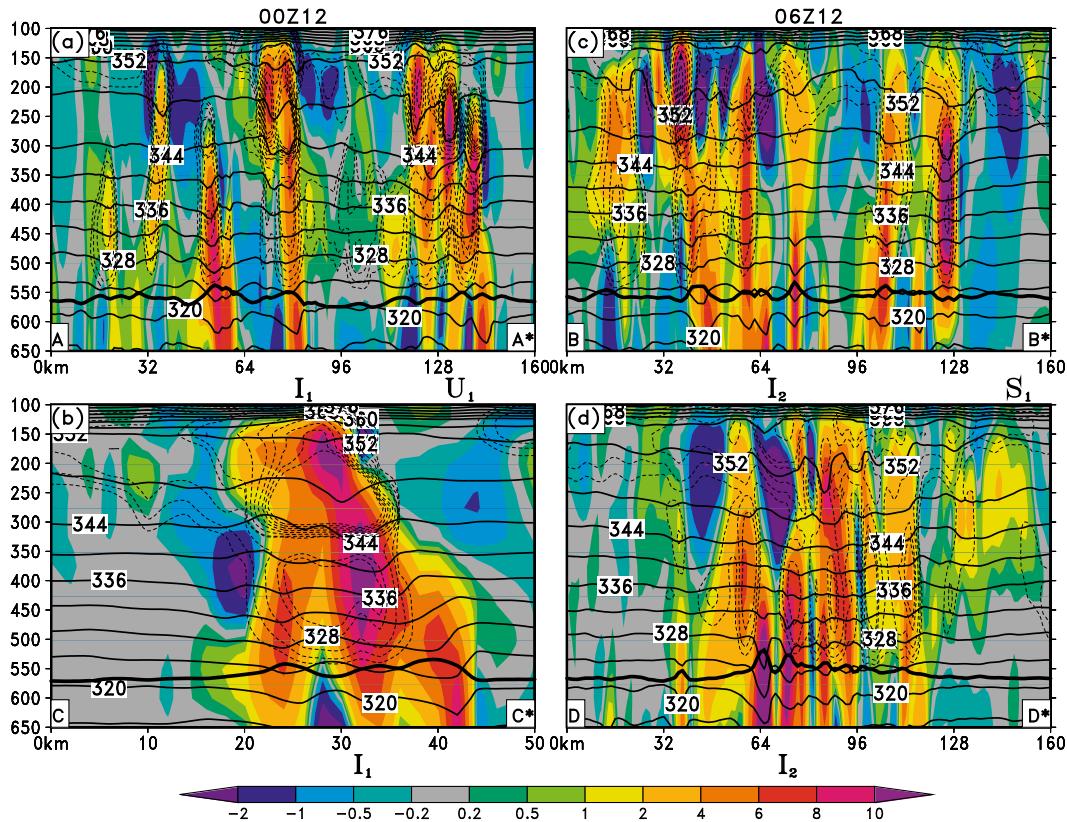


FIG. 13. (a)–(d) Vertical cross sections of simulated vertical velocity (shaded,  $\text{m s}^{-1}$ ), potential temperature (black contours at interval of 4K), cloud ice mixing ratio (dashed contours at 0.001, 0.002, 0.004, 0.008, 0.01, 0.02, 0.03, 0.04, 0.05, 0.06, and  $0.07 \text{ g kg}^{-1}$ ) and freezing level (thick black line) for 0000 [(a) A–A\* and (b) C–C\*] and 0600 [(c) B–B\* and (d) D–D\*] UTC 12 Sep with the cross-section locations given in Fig. 12 for their respective times. The letters have the same meaning as in Fig. 12, representing the approximate locations of the respective feature. Data from the WRF 1-km-resolution domain were used to create the vertical cross sections.

some cells characterized by upward velocities in excess of  $10 \text{ m s}^{-1}$  in the 275–175-hPa layer. Surrounding these CBs, compensating subsidence (blue shadings) occurs in nearly indistinguishable storm-scale outflow. Directly collocated with the CBs are large cloud ice mixing ratios and warm temperatures within the 275–175-hPa layer (Fig. 12b). This collocation suggests that these warm temperatures are associated with the latent heat of freezing and deposition as cloud water freezes after being transported upward across the  $0^\circ\text{C}$  level and more water vapor is deposited on cloud ice particles aloft.<sup>4</sup> However, these heating elements are localized to the outflow generated by individual CBs, which are sporadically located within the meso- $\beta$  surface low.

<sup>4</sup>Note that herein we distinguish that diabatic heating, which tends to accelerate updrafts, from the warming caused by compensating subsidence since the former is often more transient than the latter.

Vertical cross sections through the surface mesolow show that CBs transport cloud water above the freezing level with heating in their cores (Figs. 13a,b). At the intersection of the two cross sections (“I<sub>1</sub>”), a CB extending from the  $0^\circ\text{C}$  level (thick black line) to 100 hPa with upward velocities in excess of  $10 \text{ m s}^{-1}$  is transporting large ice content to the upper troposphere. This characteristic is also found in the core region of CB U<sub>1</sub>, but with cloud ice mixing ratios much larger in the 275–150-hPa layer. The presence of such high cloud ice content near the tropopause suggests that the heating in this layer is more a result of the depositional growth of ice rather than freezing, which is more efficient at heating the environment [i.e.,  $2839 \text{ J g}^{-1}$  for the former versus  $333 \text{ J g}^{-1}$  for the latter, Rogers and Yau (1989)]. This heating tends to accelerate updrafts and reduce the static stability of the upper troposphere (which also reduces the Rossby radius of deformation). While heating due to freezing is certainly taking place, this heating will be confined closer to the  $0^\circ\text{C}$  level and have a smaller

impact (but still important) on the thermodynamic changes in the upper troposphere.

Figure 12c shows the deepening and expansion of the meso- $\alpha$  MSLP falls and meso- $\beta$  surface low within a much more broad area of alternating upward and downward motions in the upper troposphere at 0600 UTC 12 September. Embedded within the meso- $\beta$ -scale surface low are meso- $\gamma$ -scale  $P_{\text{MIN}}$  associated with both convective bursts as well as compensating subsidence warming. An example of surface pressure falls induced by subsidence warming is marked by “S<sub>1</sub>” in Fig. 12c while an example of a closed low induced by subsidence warming occurs at the intersection of the two cross sections (“I<sub>2</sub>”). The aggregation of individual convective cells into a mesoscale convective system along the low-level critical latitude (Figs. 10e–h) has generated a meso- $\alpha$ -scale outflow (cf. Figs. 10d and 12c), which expands the cloud ice particles over a meso- $\alpha$ -scale area (Fig. 12d). This allows for deposition and freezing to occur over a larger area, expanding the upper-level warming into the feature seen in Figs. 10d and 12d. The storm-scale outflow is compensated by the development of a closed circulation at 925 hPa with pronounced convergence taking place into the center of the circulation (Fig. 12d). Comparing Figs. 12c and 12d, one can easily see the similar spatial patterns between the warming in the 275–175-hPa layer and the developing meso- $\beta$  surface low. Given the prior evidence (Figs. 9–12), it is not a stretch to believe that the warming aloft is responsible for the meso- $\beta$ -scale low and meso- $\alpha$ -scale surface pressure falls during the early hours of the simulated SI.

Figures 13c and 13d show the same fields as those in the left column except for at 0600 UTC 12 September. High cloud ice mixing ratios continue to be prevalent with a notable warming of the 275–150-hPa layer. This warming is exemplified by changes to the vertical location of the 352-K isentropic contour, which initially resides approximately near 150 hPa at 0000 UTC 12 September, but dips to near 200 hPa as the static stability of the upper troposphere reduces at 0600 UTC 12 September (Figs. 13c,d). While individual CBs are still evident at 0600 UTC 12 September, the notable change from 0000 UTC 12 September is near the center of the storm (“I<sub>2</sub>”) with compensating subsidence in excess of  $2 \text{ m s}^{-1}$  inducing warming (Figs. 13c,d). A second region of compensating subsidence warming is seen on the flank of the meso- $\beta$  surface low, as marked by “S<sub>1</sub>” in Fig. 13c. This characteristic hints at the increasing role of subsidence warming associated with an organized MCS.

It is evident that the majority of the upper-tropospheric warming is resultant from latent heating due to deposition and freezing during the early stages of simulated SI.

While we attribute the upper-tropospheric warming to a combination of diabatic heating and compensating subsidence warming, with the prior more important than the latter, the obvious rebuttal to this notion is the transient nature of the heating. Certainly, latent heating is a transient feature that is realized through convection, its positive buoyancy, and the initial gravity wave response to disperse the heating. However, it is quite evident that regardless of an “adjustment period” by which gravity waves try to disperse the heating initially, the warming survives any adjustment period that results in the system-scale signature as shown in Figs. 10 and 11. Elaborating on this further, Figs. 14a–c show the 600-hPa comoving streamlines (black), 275–175-hPa layer-averaged comoving streamlines (gray), and the Rossby radius of deformation (circle). In addition, a time series of the Rossby radius of deformation,  $L_R = NH/\eta$ , where  $N$  is the Brunt Väisälä frequency,  $H$  is the scale height, and  $\eta$  is the absolute vorticity with the calculation for  $L_R$ , is given in Fig. 14d, showing a decrease in  $L_R$  takes place just prior to and after 0600 UTC 12 September. This reduction is consistent with the intensification of low-level cyclonic vorticity (Fig. 11a, Frank 1987) and the reduction of static stability in the upper troposphere (Fig. 13).

For the entire 9-h period in Figs. 14a–c, the 600-hPa comoving circulation is on the order of or greater than the circumference created by  $L_R$ . More importantly, the storm-scale outflow in the upper-troposphere extends beyond  $L_R$ , allowing for the accumulation of the warming seen in Figs. 10–13 as the velocity field adjusts to the mass perturbations. It is evident that near the  $L_R$  the outflow shows geostrophic adjustment, with a bend of the streamlines to the right. At 0000 UTC 12 September, when the system-scale outflow is less prevalent and  $L_R$  is at its largest of the three times compared, the warming struggles to become a system-scale signature (Figs. 12a,b). This quickly changes as a mesoscale convective system becomes well organized (Figs. 10e–h) and a system-scale outflow begins to extend to near  $L_R$  in the hours prior to the simulated TD Julia (Fig. 14b). While the storm-scale inertial stability is low (as evidenced in the streamline analyses in Figs. 10a–d and 14a–c), the reduction of  $L_R$  enables the accumulation of the upper-level warming in the core region. It is important for a storm-scale outflow to be present to expand the warming outward over a meso- $\alpha$ -scale area since larger-scale warming is able to induce meaningful, similar sized surface pressure falls. This, however, must be complemented by a reduction of  $L_R$  (or an  $L_R$  already smaller than the system-scale outflow) to ensure the warming is not dispersed away from the storm center.

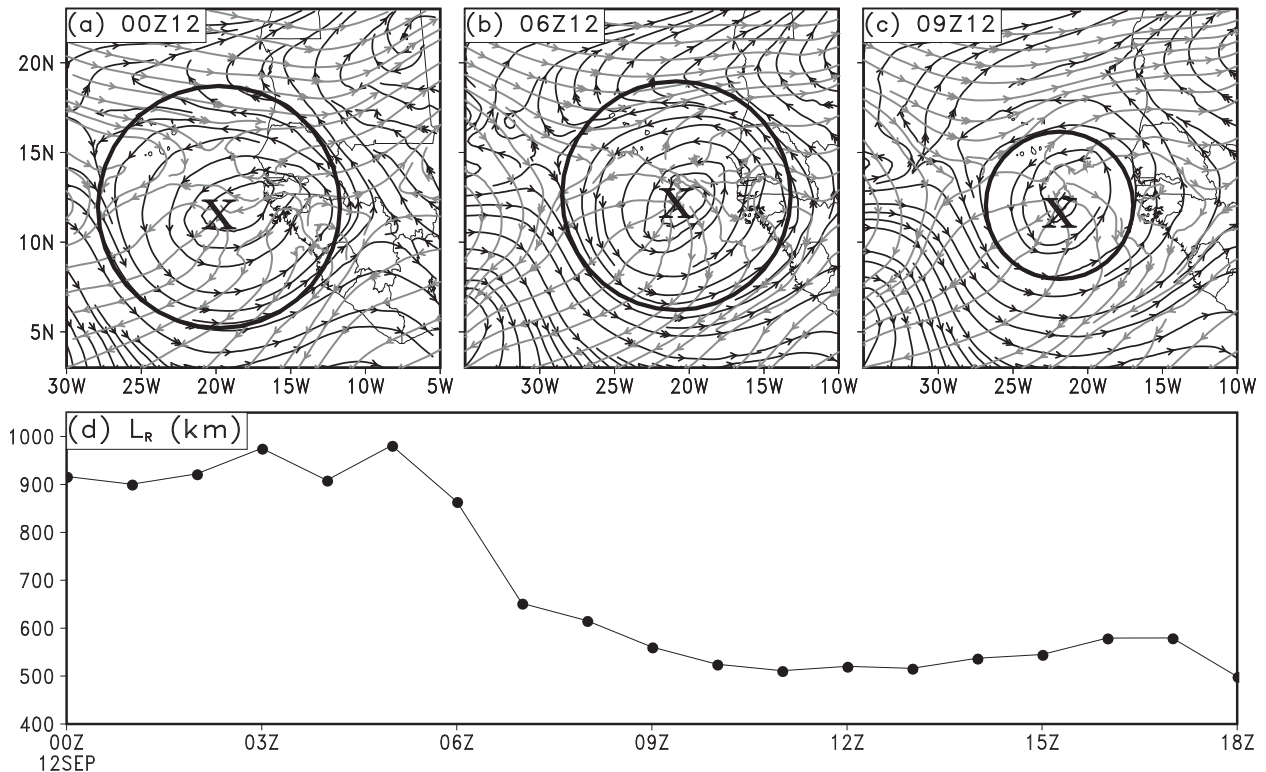


FIG. 14. (a)–(c) Simulated 600-hPa comoving streamlines (black) and layer-averaged 275–175-hPa comoving streamlines (gray) with the Rossby radius of deformation (black circle) and storm center (“X”) overlaid for 0000, 0600, and 0900 UTC 12 Sep, respectively. (d) Time series of the Rossby radius of deformation ( $L_R = NH/\eta$ ) from 0000 to 1800 UTC 12 Sep calculated using  $100 \text{ km} \times 100 \text{ km}$  area-averaged data from the 3-km-resolution WRF simulation. ( $\eta$  is calculated using the layer-averaged absolute vorticity between 1000 and 400 hPa, capturing nearly all the vorticity growth of the developing disturbance as shown in Fig. 11.  $N$  is calculated using  $N = \sqrt{(g/\bar{\theta})d\theta/dz}$ , where  $\bar{\theta}$  is the area-averaged 1000-hPa potential temperature,  $d\theta/dz$  is given by the differential of 150- and 1000-hPa potential temperatures and height surfaces, and  $g$  is the gravitational constant.  $H$  is calculated using  $H = R\bar{T}/g$ , where  $\bar{T}$  is the average temperature between 1000 and 150 hPa.  $R$  is the gas constant for dry air, and  $g$  is the gravitational constant.) Data from the WRF 9-km-resolution domain were used to create (a)–(c).

## 5. Summary and conclusions

In this study, we have examined the genesis of Hurricane Julia (2010) within an African easterly wave having an initially vertically tilted closed circulation. This AEW could be traced back to 96 h prior to genesis as a well-defined midlevel circulation. The genesis of Julia occurred shortly after the AEW moved offshore and was characterized by significant deepening (within 9 h) in MSLP and the rapid growth of a low-level vortex. The generation of the LLV can be tied to the concurrent development of deep convection and its generated vortices, upper-tropospheric warming, a meso- $\beta$ -scale surface low, and meso- $\alpha$ -scale MSLP falls. These features are protected by the AEW through ideas similar to the marsupial pouch paradigm and its low-level critical latitude.

Our model results validate the previous hypotheses that the low-level critical latitude is a preferred location

for the initiation and organization of deep convection (including convective bursts) and the development of meso- $\beta$ -scale surface lows and vortices. It is shown that convective cells and CBs reside along the AEW critical latitude during onset of the simulated significant intensification. They rapidly transport water vapor and cloud hydrometeors above the  $0^\circ\text{C}$  level, heating the upper troposphere via the latent heat of freezing and deposition. The localized diabatic heating associated with individual convective cells appears to account for the formation of numerous meso- $\beta$ - and meso- $\gamma$ -scale vortices and surface lows. As the convective cells and mesovortices aggregate, a meso- $\beta$ -scale surface low and a low-level vortex become the dominant mesoscale features within the AEW. The LLV forms through vortex stretching as a result of the presence of deep convection, enhanced PBL convergence associated with the meso- $\beta$  surface low, and the conglomeration of mesovortices along the low-level AEW critical latitude.

As deep convection intensifies and aggregates into a mesoscale convective system along the AEW critical latitude, a storm-scale outflow develops aloft, resulting in a meso- $\alpha$ -scale area of high cloud ice content and upper-level warming. The outward expansion of the warmth during the early stages of SI is made possible by latent heating due to deposition and freezing being expanded by the storm-scale outflow beyond the  $L_R$ . Furthermore,  $L_R$  decreases with time as a result of reduced static stability in the upper troposphere and increased cyclonic vorticity in the lower troposphere. With the widespread upper-tropospheric warming, meso- $\alpha$ -scale MSLP falls are hydrostatically induced, creating a low-level cyclonic disturbance needed for stage 1 of tropical cyclogenesis development described in the introduction. It is evident that the meso- $\alpha$ -scale MSLP falls are closely tied to the thermodynamic changes and divergent outflows in the upper troposphere that, in turn, are inherently tied to the development of deep convection along the low-level critical latitude of the AEW. Clearly, the meso- $\alpha$ -scale MSLP falls tend to enhance the PBL convergence for the bottom-up growth of TC-scale rotation.

To summarize, the key elements to this sequence of events are (i) the initiation, intensification, and aggregation of deep convection and its generated vortices along the AEW low-level critical latitude and (ii) the development of the upper- or high-level warmth, a storm-scale outflow beyond the Rossby radius of deformation, and meso- $\alpha$ -scale MSLP falls. Without either of these, the genesis of the simulated Julia may not occur.

Further work needs to explore this sequence of events for other cases. In particular, the importance of convective development along the critical latitude and its relationship to the upper-level warming needs to be further explored. We postulate that the warming can only exist when a persistent storm-scale outflow develops with convective development along the AEW low-level critical latitude. That being said, we have already conducted ensemble simulations on the TCG of Hurricane Julia using 20 members at the finest resolution of 1 km. The results from those members will certainly lend insight into the plausibility of the idealized implications of upper-level warming in relation to deep convection, the LLV and the theories presented in the marsupial pouch paradigm.

*Acknowledgments.* This work was supported by NASA Headquarters under the NASA Earth and Space Science Fellowship Program Grant NNX11AP29H. Model simulations were performed at the NASA High-End Computing (HEC) Program through the NASA

Center for Climate Simulation (NCCS) at Goddard Space Flight Center. The ERA-Interim data for this study were from the Research Data Archive (RDA) maintained by the Computational and Information Systems Laboratory (CISL) at the National Center for Atmospheric Research, which is sponsored by the National Science Foundation. Satellite data was provided by the Cooperative Institute for Meteorological Satellite Studies (CIMSS) Tropical Cyclone Image Archive, University of Wisconsin. TRMM data set 3B42 version 7A was provided by NASA GSFC Mirador website available from [http://mirador.gsfc.nasa.gov/collections/TRMM\\_3B42\\_007.shtml](http://mirador.gsfc.nasa.gov/collections/TRMM_3B42_007.shtml).

#### REFERENCES

- Berry, G. J., and C. Thorncroft, 2005: Case study of an intense African easterly wave. *Mon. Wea. Rev.*, **133**, 752–766.
- Beven, J. L., and C. L. Landsea, 2010: Hurricane Julia (AL122010) 12–20 September 2010. National Hurricane Center Tropical Cyclone Rep., 17 pp. [Available online at [http://www.nhc.noaa.gov/pdf/TCR-AL122010\\_Julia.pdf](http://www.nhc.noaa.gov/pdf/TCR-AL122010_Julia.pdf).]
- Bister, M., and K. A. Emanuel, 1997: The genesis of Hurricane Guillermo: TEXMEX analyses and a modeling study. *Mon. Wea. Rev.*, **125**, 2662–2682.
- Braun, S. A., and Coauthors, 2013: NASA's Genesis and Rapid Intensification Processes (GRIP) field experiment. *Bull. Amer. Meteor. Soc.*, **94**, 345–363.
- Burpee, R. W., 1972: The origin and structure of easterly waves in the lower troposphere of North America. *J. Atmos. Sci.*, **29**, 77–90.
- Charney, J. G., and M. E. Stern, 1962: On the stability of internal baroclinic jets in a rotating atmosphere. *J. Atmos. Sci.*, **19**, 159–172.
- Chen, H., and D.-L. Zhang, 2013: On the rapid intensification of Hurricane Wilma (2005). Part II: Convective bursts and the upper-level warm core. *J. Atmos. Sci.*, **70**, 146–172.
- Dudhia, J., 1989: Numerical study of convection observed during the winter monsoon experiment using a mesoscale two-dimensional model. *J. Atmos. Sci.*, **46**, 3077–3107.
- Dunkerton, T. J., M. T. Montgomery, and Z. Wang, 2009: Tropical cyclogenesis in a tropical wave critical layer: Easterly waves. *Atmos. Chem. Phys.*, **9**, 5587–5646.
- Frank, N. L., 1970: Atlantic tropical systems of 1969. *Mon. Wea. Rev.*, **98**, 307–314.
- Frank, W. M., 1987: Tropical cyclone formation. *Global View of Tropical Cyclones*, R. L. Elsberry, Ed., Office of Naval Research, 53–90.
- Gray, W. M., 1968: Global view of the origin of tropical disturbances and storms. *Mon. Wea. Rev.*, **96**, 669–700.
- Harr, P. A., R. L. Elsberry, and J. C. L. Chan, 1996: Transformation of a large monsoon depression to a tropical storm during TCM-93. *Mon. Wea. Rev.*, **124**, 2625–2643.
- Hendricks, E. A., M. T. Montgomery, and C. A. Davis, 2004: The role of vortical hot towers in the formation of Tropical Cyclone Diana (1984). *J. Atmos. Sci.*, **61**, 1209–1232.
- Hogsett, W., and D.-L. Zhang, 2010: Genesis of Typhoon Chanchu (2006) from a westerly wind burst associated with the MJO. Part I: Evolution of a vertically tilted precursor vortex. *J. Atmos. Sci.*, **67**, 3774–3792.

- Hopsch, S. B., C. D. Thorncroft, and K. R. Tyle, 2010: Analysis of African easterly wave structures and their role in influencing tropical cyclogenesis. *Mon. Wea. Rev.*, **138**, 1399–1419.
- Houze, R. A., W.-C. Lee, and M. M. Bell, 2009: Convective contribution to the genesis of Hurricane Ophelia (2005). *Mon. Wea. Rev.*, **137**, 2778–2800.
- Hoxit, L. R., C. Chappell, and J. Fritch, 1976: Formation of mesolows or pressure troughs in advance of cumulonimbus clouds. *Mon. Wea. Rev.*, **104**, 1419–1428.
- Kain, J. S., 2004: The Kain–Fritsch convective parameterization: An update. *J. Appl. Meteor.*, **43**, 170–181.
- , and J. M. Fritsch, 1990: A one-dimensional entraining/detraining plume model and its application in convective parameterization. *J. Atmos. Sci.*, **47**, 2784–2812.
- Karyampudi, V. M., and H. F. Pierce, 2002: Synoptic-scale influence of the Saharan air layer on tropical cyclogenesis over the eastern Atlantic. *Mon. Wea. Rev.*, **130**, 3100–3128.
- Kieu, C. Q., and D.-L. Zhang, 2009: Genesis of Tropical Storm Eugene (2005) from merging vortices associated with ITCZ breakdowns. Part II: Roles of vortex merger and ambient potential vorticity. *J. Atmos. Sci.*, **66**, 1980–1996.
- Li, T., and B. Fu, 2006: Tropical cyclogenesis associated with Rossby wave energy dispersion of a preexisting typhoon. Part I: Satellite data and analyses. *J. Atmos. Sci.*, **63**, 1377–1389.
- , X. Ge, B. Wang, and Y. Zhu, 2006: Tropical cyclogenesis associated with Rossby wave energy dispersion of a preexisting typhoon. Part II: Numerical simulations. *J. Atmos. Sci.*, **63**, 1390–1409.
- Mlawer, E. J., S. J. Taubman, P. D. Brown, M. J. Iacono, and S. A. Clough, 1997: Radiative transfer for inhomogeneous atmospheres: RRTM, a validated correlated-k model for the longwave. *J. Geophys. Res.*, **102** (D14), 16 663–16 682.
- Montgomery, M. T., M. E. Nicholls, T. A. Cram, and A. B. Saunders, 2006: A vortical hot tower route to tropical cyclogenesis. *J. Atmos. Sci.*, **63**, 355–386.
- , L. L. Lussier III, R. W. Moore, and Z. Wang, 2010: The genesis of Typhoon Nuri as observed during the Tropical Cyclone Structure 2008 (TCS-08) field experiment—Part 1: The role of the easterly wave critical layer. *Atmos. Chem. Phys.*, **10**, 9879–9900.
- , and Coauthors, 2012: The Pre-Depression Investigation of Cloud-Systems in the Tropics (PREDICT) experiment: Scientific basis, new analysis tools, and some first results. *Bull. Amer. Meteor. Soc.*, **93**, 153–172.
- Noh, Y. W., W. G. Cheon, S. Y. Hong, and S. Raasch, 2003: Improvement of the k-profile model for the planetary boundary layer based on large eddy simulation data. *Bound.-Layer Meteor.*, **9**, 401–427.
- Nolan, D. S., 2007: What is the trigger for tropical cyclogenesis? *Aust. Meteor. Mag.*, **56**, 241–266.
- Reynolds, R. W., T. M. Smith, C. Lui, D. B. Chelton, K. S. Casey, and M. G. Schlax, 2007: Daily high-resolution blended analyses for sea surface temperature. *J. Climate*, **20**, 5473–5496.
- Riehl, H., and J. S. Malkus, 1958: On the heat balance in the equatorial trough zone. *Geophysica*, **6**, 503–538.
- Ritchie, E. A., and G. J. Holland, 1997: Scale interactions during the formation of Typhoon Irving. *Mon. Wea. Rev.*, **125**, 1377–1396.
- Rogers, R. R., and M. K. Yau, 1989: *A Short Course in Cloud Physics*. 3rd ed. Butterworth-Heinemann, 290 pp.
- Schreck, C. J., J. Molinari, and A. Ayyer, 2012: A global view of equatorial waves and tropical cyclogenesis. *Mon. Wea. Rev.*, **140**, 774–788.
- Simpson, J., J. B. Halverson, B. S. Ferrier, W. A. Petersen, R. H. Simpson, R. Blakeslee, and S. L. Durden, 1998: On the role of “hot towers” in tropical cyclone formation. *Meteor. Atmos. Phys.*, **67**, 15–35.
- Sippel, J. A., J. W. Nielsen-Gammon, and S. E. Allen, 2006: The multiple-vortex nature of tropical cyclogenesis. *Mon. Wea. Rev.*, **134**, 1796–1814.
- Skamarock, W. C., J. B. Klemp, J. Dudhia, D. O. Gill, D. M. Barker, W. Wang, and J. G. Powers, 2005: A description of the advanced research WRF version 2. NCAR Tech. Note NCAR/TN-468+STR, 88 pp.
- Thompson, G., R. M. Rasmussen, and K. Manning, 2004: Explicit forecasts of winter precipitation using an improved bulk microphysics scheme. Part I: Description and sensitivity analysis. *Mon. Wea. Rev.*, **132**, 519–542.
- , P. R. Field, R. M. Rasmussen, and W. D. Hall, 2008: Explicit forecasts of winter precipitation using an improved bulk microphysics scheme. Part II: Implementation of a new snow parameterization. *Mon. Wea. Rev.*, **136**, 5095–5115.
- Thorncroft, C., and K. Hodges, 2001: African easterly wave variability and its relationship to Atlantic tropical cyclone activity. *J. Climate*, **14**, 1166–1179.
- Vizy, E. K., and K. H. Cook, 2009: Tropical storm development from African easterly waves in the eastern Atlantic: A comparison of two successive waves using a regional model as part of NASA AMMA 2006. *J. Atmos. Sci.*, **66**, 3313–3334.
- Wang, Z., 2012: Thermodynamic aspects of tropical cyclone formation. *J. Atmos. Sci.*, **69**, 2433–2451.
- , M. T. Montgomery, and T. J. Dunkerton, 2010a: Genesis of pre-Hurricane Felix (2007). Part I: The role of the easterly wave critical layer. *J. Atmos. Sci.*, **67**, 1711–1729.
- , —, and —, 2010b: Genesis of pre-Hurricane Felix (2007). Part II: Warm core formation, precipitation evolution, and predictability. *J. Atmos. Sci.*, **67**, 1730–1744.
- , —, and C. Fritz, 2012: A first look at the structure of the wave pouch during the 2009 PREDICT-GRIP dry runs over the Atlantic. *Mon. Wea. Rev.*, **140**, 1144–1163.
- Zhang, D.-L., and J. M. Fritsch, 1987: Numerical simulation of the meso-beta scale structure and evolution of the 1977 Johnston flood. Part II: Inertially stable warm-core vortex and the mesoscale convective complex. *J. Atmos. Sci.*, **44**, 2593–2612.
- , and N. Bao, 1996: Oceanic cyclogenesis as induced by a mesoscale convective system moving offshore. Part II: Genesis and thermodynamic transformation. *Mon. Wea. Rev.*, **124**, 2206–2226.
- , and L. Zhu, 2012: Roles of upper-level processes in tropical cyclogenesis. *Geophys. Res. Lett.*, **39**, L17804, doi:10.1029/2012GL053140.